Submitted to ApJ
Preprint typeset using LaTeX style emulateapj v. 5/2/11

arXiv:1510.07043v2 [astro-ph.IM] 21 Apr 2016

BAYESIAN REDSHIFT CLASSIFICATION OF EMISSION-LINE GALAXIES WITH PHOTOMETRIC EQUIVALENT WIDTHS

Andrew S. Leung[1,2], Viviana Acquaviva[3], Eric Gawiser[1], Robin Ciardullo[4,5], Eiichiro Komatsu[6,7], A.I. Malz[8], Gregory R. Zeimann[4,5,2], Joanna S. Bridge[4,5], Niv Drory[9], John J. Feldmeier[10], Steven L. Finkelstein[2], Karl Gebhardt[2], Caryl Gronwall[4,5], Alex Hagen[4,5], Gary J. Hill[2,9], and Donald P. Schneider[4,5]

Submitted to ApJ

ABSTRACT

We present a Bayesian approach to the redshift classification of emission-line galaxies when only a single emission line is detected spectroscopically. We consider the case of surveys for high-redshift Lyα-emitting galaxies (LAEs), which have traditionally been classified via an inferred rest-frame equivalent width ($W_{\mathrm{Ly}\alpha}$) greater than 20 Å. Our Bayesian method relies on known prior probabilities in measured emission-line luminosity functions and equivalent width distributions for the galaxy populations, and returns the probability that an object in question is an LAE given the characteristics observed. This approach will be directly relevant for the Hobby–Eberly Telescope Dark Energy Experiment (HETDEX), which seeks to classify $\sim 10^6$ emission-line galaxies into LAEs and low-redshift [O II] emitters. For a simulated HETDEX catalog with realistic measurement noise, our Bayesian method recovers 86 % of LAEs missed by the traditional $W_{\mathrm{Ly}\alpha} > 20$ Å cutoff over $2 < z < 3$, outperforming the equivalent width (EW) cut in both contamination and incompleteness. This is due to the method's ability to trade off between the two types of binary classification error by adjusting the stringency of the probability requirement for classifying an observed object as an LAE. In our simulations of HETDEX, this method reduces the uncertainty in cosmological distance measurements by 14 % with respect to the EW cut, equivalent to recovering 29 % more cosmological information. Rather than using binary object labels, this method enables the use of classification probabilities in large-scale structure analyses. It can be applied to narrowband emission-line surveys as well as upcoming large spectroscopic surveys including *Euclid* and WFIRST.

Subject headings: cosmology: cosmological parameters – cosmology: observations – galaxies: distances and redshifts – galaxies: emission lines – galaxies: high-redshift – methods: statistical

1. INTRODUCTION

The Hobby–Eberly Telescope Dark Energy Experiment[11] (HETDEX) will obtain redshifts for approximately a million Lyα-emitting galaxies (LAEs) in its upcoming wide-field survey and to determine the local Hubble expansion rate, angular diameter distance (d_A), and the growth of structure in the $1.9 < z < 3.5$ universe (Hill et al. 2008). To achieve its science goals, HETDEX requires an accurate classifier to identify LAEs and discard contaminants (primarily $z < 0.5$ [O II] emitters) from the statistical LAE sample.

Lyα is a spectral feature produced by the transition of neutral hydrogen atoms from the first excited state to the ground state ($n = 2 \rightarrow 1$), with a rest-frame wavelength of 1216 Å. The Visible Integral-field Replicable Unit Spectrograph (VIRUS), currently being deployed at the Hobby–Eberly Telescope (HET), has a spectral range of 3500–5500 Å (Hill & HETDEX Collaboration 2015), making spectroscopic detections of Lyα possible between redshifts $1.88 < z < 3.52$. This capability enables the primary science goal of the HETDEX survey, the measurement of the expansion history of the universe (Hill et al. 2008; Adams et al. 2011), by constraining cosmological parameters from the observed signature of baryon acoustic oscillations (BAO) in the power spectrum of LAE redshifts and positions (Seo & Eisenstein 2003; Blake & Glazebrook 2003; Hu & Haiman 2003; Seo & Eisenstein 2007; Koehler et al. 2007; Shoji et al. 2009). Lyα is usually the strongest line, therefore near the survey limit, where most of the targets lie, the VIRUS spectra will have only one detected emission line.

Another prominent emission line feature in galaxy spectra is the [O II] doublet at ~ 3726 Å and ~ 3729 Å,

[1] Department of Physics and Astronomy, Rutgers, The State University of New Jersey, Piscataway, New Jersey 08854, USA; gawiser@physics.rutgers.edu
[2] Department of Astronomy, The University of Texas at Austin, Austin, Texas 78712, USA; leung@astro.as.utexas.edu
[3] Department of Physics, New York City College of Technology, The City University of New York, Brooklyn, New York 11201, USA; vacquaviva@citytech.cuny.edu
[4] Department of Astronomy and Astrophysics, The Pennsylvania State University, University Park, Pennsylvania 16802, USA
[5] Institute for Gravitation and the Cosmos, The Pennsylvania State University, University Park, Pennsylvania 16802, USA
[6] Max-Planck-Institut für Astrophysik, 85740 Garching bei München, Germany
[7] Kavli Institute for the Physics and Mathematics of the Universe (Kavli IPMU, WPI), Todai Institutes for Advanced Study, The University of Tokyo, Kashiwa 277-8583, Japan
[8] Center for Cosmology and Particle Physics, Department of Physics, New York University, New York, New York 10003, USA
[9] McDonald Observatory, The University of Texas at Austin, Austin, Texas 78712, USA
[10] Department of Physics and Astronomy, Youngstown State University, Youngstown, Ohio 44555, USA
[11] http://www.hetdex.org

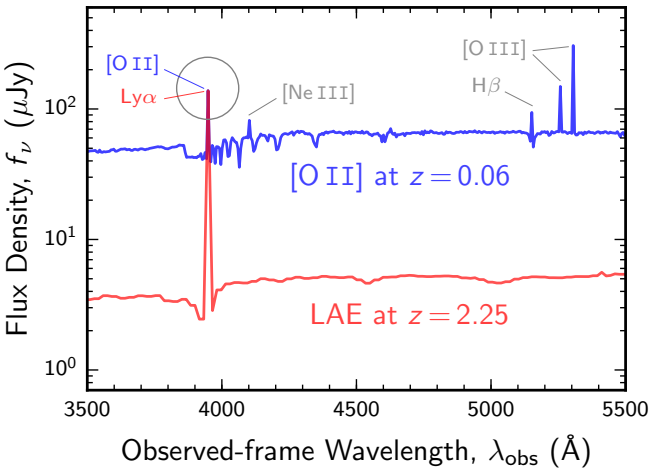

Figure 1. The spectra of two model galaxies over the spectral range of HETDEX are shown in this example. The Lyα line in the spectrum of the high-redshift galaxy (red) is observed at the same wavelength as the unresolved [O II] doublet from a low-redshift galaxy (blue) in the survey foreground. Intensity of the primary emission line (indicated by the gray circle) is identical for the two galaxies depicted, but the continuum flux densities of the two spectra are different. The LAE in this example, as is typically the case, has a much larger equivalent width than the [O II] emitter depicted. The use of [Ne III], Hβ and [O III] lines in applicable cases as additional spectral information for Bayesian classification is discussed in § 3.3.

a pair of atomic transitions for the decay of singly ionized oxygen. Galaxies with strong [O II] emission from $z < 0.476$ will also be identified by HETDEX as a single-line detection within its spectral range, as the [O II] $\lambda 3727$ doublet is separated by 2.5 Å (rest frame; Osterbrock 1974) and cannot be resolved by the VIRUS instrument (spectral resolution: 5.7 Å). Distinguishing LAEs targeted by HETDEX from low-redshift [O II] emitters therefore represents a challenge in a blind spectroscopic survey when only one emission line is detected (Adams et al. 2011).

Figure 1 illustrates this classification problem. In the example, a high-redshift LAE and a foreground [O II] emitter are detected via their primary emission lines observed at the same wavelength, with identical fluxes measured for the detected lines. In order to make an accurate redshift classification, we need to consider additional information available in our measurements. narrowband selection for strong Lyα emission in the literature typically requires LAEs to have rest-frame equivalent width ($W_{\mathrm{Ly}\alpha}$) greater than 20 Å (e.g., Cowie & Hu 1998; Gronwall et al. 2007). This equivalent width (EW) method is effective in limiting the misclassification of [O II] emitters as LAEs (Gawiser et al. 2006) at redshift $2 < z < 3$, at the expense of having an incomplete sample of LAEs. However, fractional contamination in the LAE sample increases rapidly with redshift due to two concurrent factors: the rapid rise in the volume occupied by [O II] emitters and the increase in their average intrinsic equivalent widths (Hogg et al. 1998; Ciardullo et al. 2013). Using the simple EW cut reduces the purity and completeness of a statistical sample of objects classified as LAEs and thus the precision with which HETDEX will be able to measure the evolution of dark energy (Komatsu 2010).

The distributions of line luminosity and equivalent widths have been measured for emission-line selected samples of LAEs (e.g., Shimasaku et al. 2006; Gronwall et al. 2007; Ouchi et al. 2008; Guaita et al. 2010; Ciardullo et al. 2012) and [O II] emitters (Ciardullo et al. 2013) over the spectral range of the HETDEX survey. In addition, the equivalent width distribution of [O II] emitters in the local universe has been extremely well measured using both continuum and emission-line selected galaxy samples (Blanton & Lin 2000; Gallego et al. 1996, 2002). With these distribution functions as prior probabilities, we can compute the relative likelihood that a detected emission-line object is an LAE or an [O II] emitter given its observed characteristics.

We explore this Bayesian approach to classifying emission-line galaxies as a means to improve the quality of the cosmological sample of LAEs. Section 2 describes our methodology, including details of the simulation of a HETDEX catalog consisting of LAEs and [O II] emitters (§ 2.1) and an overview of the statistical framework for a Bayesian method that can be used to identify LAEs in a line flux-limited sample of emission-line galaxies (§ 2.2). Section 3 presents the results of Bayesian classification of LAEs in a simulated HETDEX catalog and quantifies the improvement over the equivalent width method. Section 4 offers a discussion of our findings and their applications.

Throughout the present work, we assume a ΛCDM cosmology with $H_0 = 70\ \mathrm{km\,s^{-1}\,Mpc^{-1}}$, $\Omega_m = 0.3$, and $\Omega_\Lambda = 0.7$ (Komatsu et al. 2011; *Planck* Collaboration et al. 2015). All magnitudes are reported in the AB system (Oke & Gunn 1983).

2. METHODOLOGY

2.1. *Simulated Catalog of Emission-line Galaxies*

We simulate populations of LAEs and [O II] emitters on which to test the methods for galaxy classification. For the simulations, we specify a 300 deg^2 survey area (the size of the HETDEX spring field, roughly two-thirds of the total survey area) and a 1/4.5 filling factor to mimic the design of the upcoming HETDEX survey (Hill & HETDEX Collaboration 2015).

2.1.1. *Spectroscopic Survey Simulation*

Gronwall et al. (2007), Ciardullo et al. (2012), and Gronwall et al. (2016, in prep; hereafter `Gr16`) have measured the luminosity functions for LAE populations at $z = 2.1$ and $z = 3.1$. Using the `Gr16` luminosity functions, we simulate Lyα line luminosities via Monte Carlo simulations. We use a Schechter (1976) function of the form:

$$\Phi(L)\,dL = \phi^*\,(L/L^*)^\alpha\,\exp(-L/L^*)\,d(L/L^*)\,, \qquad (1)$$

and assume that the parameters (shown in Table 1) evolve linearly with redshift. We obtain the distribution parameters at redshifts $2.1 < z < 3.1$ by linear interpolation of the `Gr16` parameter values for $z = 2.1$ and $z = 3.1$; for simulated LAEs at $z < 2.1$ and $z > 3.1$, we linearly extrapolate the parameters. The top left panel in Figure 2 shows that our extrapolation of the `Gr16` luminosity function to $z = 3.5$ is consistent with the weakly evolving Lyα luminosity functions measured at higher redshift (Shimasaku et al. 2006; Ouchi et al. 2008; Henry et al. 2012).

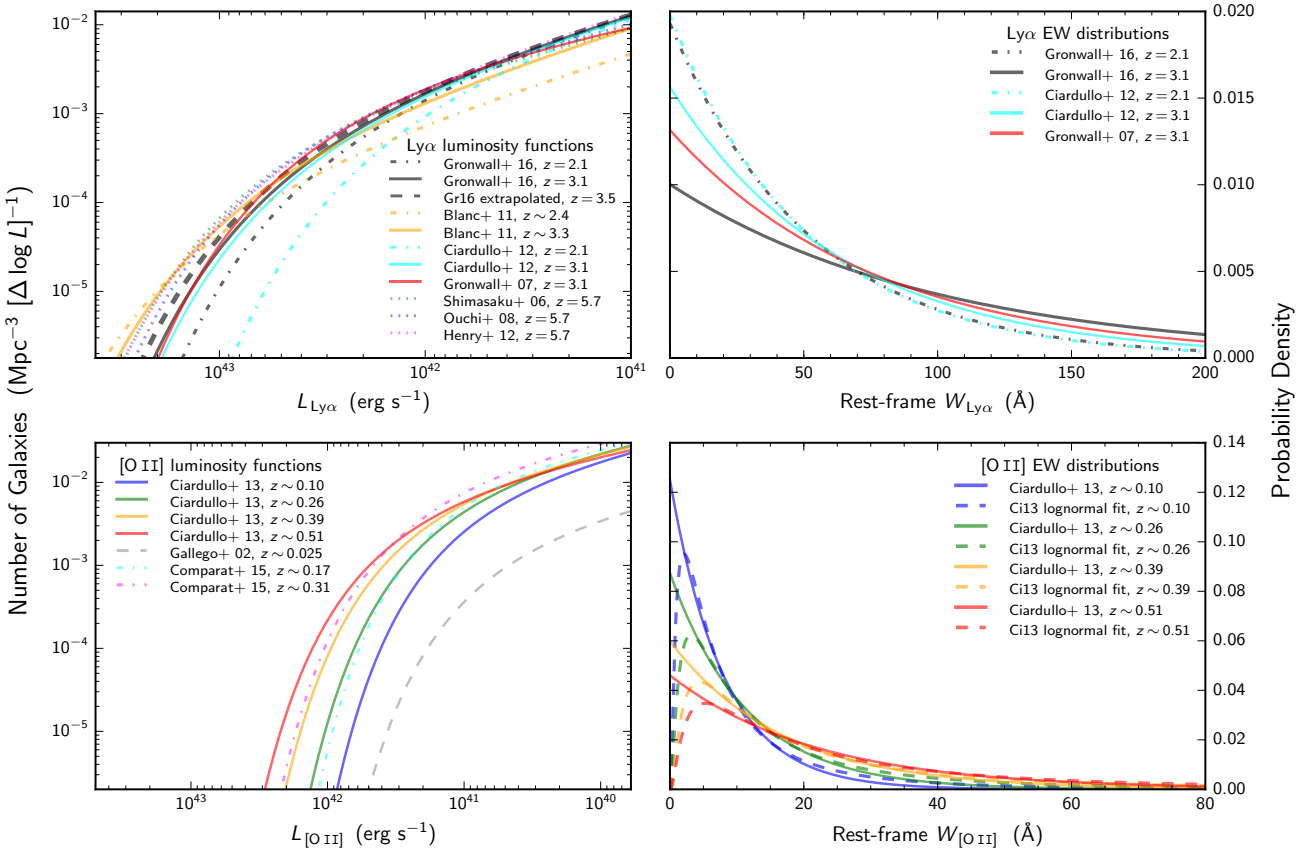
Lyα luminosity functions
Gronwall+ 16, z = 2.1
Gronwall+ 16, z = 3.1
Gr16 extrapolated, z = 3.5
Blanc+ 11, z ∼ 2.4
Blanc+ 11, z ∼ 3.3
Ciardullo+ 12, z = 2.1
Ciardullo+ 12, z = 3.1
Gronwall+ 07, z = 3.1
Shimasaku+ 06, z = 5.7
Ouchi+ 08, z = 5.7
Henry+ 12, z = 5.7
Number of Galaxies (Mpc⁻³ [Δ log L]⁻¹)
L_Lyα (erg s⁻¹)
Lyα EW distributions
Gronwall+ 16, z = 2.1
Gronwall+ 16, z = 3.1
Ciardullo+ 12, z = 2.1
Ciardullo+ 12, z = 3.1
Gronwall+ 07, z = 3.1
Rest-frame W_Lyα (Å)
Probability Density
[O II] luminosity functions
Ciardullo+ 13, z ∼ 0.10
Ciardullo+ 13, z ∼ 0.26
Ciardullo+ 13, z ∼ 0.39
Ciardullo+ 13, z ∼ 0.51
Gallego+ 02, z ∼ 0.025
Comparat+ 15, z ∼ 0.17
Comparat+ 15, z ∼ 0.31
L_[O II] (erg s⁻¹)
[O II] EW distributions
Ciardullo+ 13, z ∼ 0.10
Ci13 lognormal fit, z ∼ 0.10
Ciardullo+ 13, z ∼ 0.26
Ci13 lognormal fit, z ∼ 0.26
Ciardullo+ 13, z ∼ 0.39
Ci13 lognormal fit, z ∼ 0.39
Ciardullo+ 13, z ∼ 0.51
Ci13 lognormal fit, z ∼ 0.51
Rest-frame W_[O II] (Å)

Figure 2. Luminosity functions and equivalent width distributions for LAEs and [O II] emitters. *Upper left*: The dashed black curve is obtained by linear extrapolation of Schechter function parameters reported by Gronwall et al. (2016) out to $z = 3.5$; it is consistent with Lyα luminosity functions measured at higher redshifts (Shimasaku et al. 2006; Ouchi et al. 2008; Henry et al. 2012). *Upper right*: Lyα EW distributions assumed in simulations in the present work; Gronwall et al. (2016) parameters evolving linearly with redshift constitute our "baseline" scenario (see Table 4). *Lower right*: Dashed lines show lognormal fits at EW > 5 Å to the exponential equivalent width distributions measured by Ciardullo et al. (2013) (see § 4.1); the exponential form is used in simulations of [O II] equivalent widths in the present work. *Lower left*: [O II] luminosity functions used in our simulations (Ciardullo et al. 2013) are consistent with published results at similar redshifts (Gallego et al. 2002; Comparat et al. 2015).

The measured equivalent width distributions of LAEs have been modeled with various distributions. For our simulations, we assume an exponential form with a scale length, w_0:

$$\Psi(W)\, dW = \frac{e^{-W/w_0}}{w_0}\, dW\,. \qquad (2)$$

As with the Schechter function parameters, we assume the exponential scale lengths evolve linearly with redshift. Since previous studies have found weak or no correlation between emission-line luminosity and equivalent width (Cowie et al. 1996; Hogg et al. 1998; Gronwall et al. 2007; Ciardullo et al. 2012, 2013), we model the luminosity function and the equivalent width distribution as orthogonal functions.

The simulation of [O II] luminosities follows the same procedure as described above, with Schechter function parameters reported by Ciardullo et al. (2013, hereafter `Ci13`). The [O II] luminosity function has also been measured in studies by Gallego et al. (2002), Teplitz et al. (2003), Hippelein et al. (2003), Ly et al. (2007), Takahashi et al. (2007), and Comparat et al. (2015). For simplicity, we assume the exponential form in Equation (2) for the [O II] equivalent width distributions, with `Ci13` parameters linearly evolving with redshift.

To model the evolution of the galaxy property distributions, we choose small values of Δz for our simulations ($\Delta z = 0.01$ for LAEs; and $\Delta z = 0.005$ for [O II] emitters, whose corresponding volume elements are smaller). The total number of each type of object to be simulated in a given redshift bin is given by the product of the comoving volume of the survey area in Δz and the integral of the Schechter function above a conservative minimum flux, below which there can be no line detections on VIRUS. For each simulated object, the realized redshift and object type (LAE or [O II] emitter) determine the observed-frame wavelength ($\lambda_{\rm EL}$) of the primary simulated emission line. Since Lyα luminosity functions were measured for LAEs selected with the $W_{\rm Ly\alpha} > 20$ Å requirement (e.g., Ciardullo et al. 2012; Gronwall et al. 2016) and our Monte Carlo simulations realize equivalent widths from probability distributions that go down to 0 Å, we must correct the number density of LAEs to account for the fraction that would have $W_{\rm Ly\alpha} \leq 20$ Å.[12]

[12] The correction factor is equal to $1/e^{-20\text{Å}/w_0}$. Assuming the results in `Gr16`, the factors at $z = 2.1$ and $z = 3.1$ are 1.49 and 1.22, respectively.

Table 1
Schechter function parameters and exponential scale lengths for LAEs and [O II] emitters; parameters for fitted lognormal [O II] equivalent width distributions are shown in the far-right column

Sample			Schechter function			Exponential EW	Lognormal EW [a,b]
			α	$\log L^*$ (erg s^{-1})	$\log \phi^*$ (Mpc^{-3})	w_0 (Å)	W_0 (Å)
LAE	$z\sim2.1$	Gr16 [c]	-1.65	$42.61^{+0.17}_{-0.06}$	$-3.08^{+0.04}_{-0.06}$	50^{+5}_{-4}	—
"	"	Ci12 [d]	-1.65	$42.33^{+0.12}_{-0.12}$	$-2.86^{+0.05}_{-0.05}$	50^{+7}_{-7}	—
LAE	$z\sim3.1$	Gr16	-1.65	$42.77^{+0.10}_{-0.08}$	$-2.98^{+0.07}_{-0.06}$	100^{+28}_{-14}	—
"	"	Ci12	-1.65	$42.76^{+0.10}_{-0.10}$	$-3.17^{+0.05}_{-0.05}$	64^{+9}_{-9}	—
"	"	Gr07 [e]	-1.36	$42.66^{+0.26}_{-0.15}$	$-2.89^{+0.04}_{-0.03}$	76^{+11}_{-8}	—
[O II]	$z\sim0.10$	Ci13 [f]	-1.20	$41.07^{+0.18}_{-0.16}$	$-2.34^{+0.05}_{-0.06}$	$8.0^{+1.6}_{-1.6}$	$3.8^{+0.9}_{-0.8}$
"	$z\sim0.26$	"	-1.20	$41.29^{+0.11}_{-0.11}$	$-2.34^{+0.03}_{-0.03}$	$11.5^{+1.6}_{-1.6}$	$5.8^{+0.8}_{-0.9}$
"	$z\sim0.39$	"	-1.20	$41.50^{+0.08}_{-0.10}$	$-2.43^{+0.01}_{-0.01}$	$16.6^{+2.4}_{-2.4}$	$8.2^{+0.9}_{-1.0}$
"	$z\sim0.51$	"	-1.20	$41.68^{+0.08}_{-0.12}$	$-2.54^{+0.01}_{-0.01}$	$21.5^{+3.3}_{-3.3}$	$10.1^{+1.1}_{-1.2}$

[a] Lognormal distribution parameter σ_W is fixed at 1.1 for all redshifts $z_{[\mathrm{O\,II}]}$; see Equation (28).
[b] The consequences of using lognormally distributed [O II] EWs are discussed in § 4.1.
[c] Gronwall et al. (2016)
[d] Ciardullo et al. (2012)
[e] Gronwall et al. (2007)
[f] Ciardullo et al. (2013)

Other emission lines are added to the simulated spectra of [O II] emitters, based on relative line strengths as a function of metallicity (Anders & Fritze-v. Alvensleben 2003), which we assume to be one-fifth of solar for low-redshift objects in our simulations. The nearest [O II] emitters ($z\lesssim0.1$) have four other strong emission lines — [Ne III] $\lambda3869$, Hβ $\lambda4861$, [O III] $\lambda4959$, and [O III] $\lambda5007$ — that may be detected within the spectral range of HETDEX (see Figure 1), depending on the redshift.

Gaussian noise with a mean equal to zero and a standard deviation equal to one-fifth of the wavelength-dependent 5σ line flux sensitivity limit of HETDEX is added to simulated line fluxes. Subsequent to the addition of noise, simulated objects with "recorded" line fluxes that fall below the 5σ detection limit are eliminated from the "observable" sample, resulting in a 5σ line flux-limited sample of emission-line galaxies for our simulated catalog.

2.1.2. *Imaging Survey Simulation*

We explore a scenario specific to our application (HETDEX), where spectroscopic line fluxes are coupled with continuum flux densities obtained through aperture photometry on broadband imaging, resulting in measurements of *photometric* equivalent widths. Noiseless simulated emission line fluxes (f_{EL}) and observed-frame equivalent widths ($\mathrm{EW_{obs}}$) are converted into continuum flux densities ($f_{\nu,\,\mathrm{cont}}$) at the observed emission-line wavelength, as follows:

$$\mathrm{EW_{obs}} = \frac{f_{\mathrm{EL}}}{f_{\lambda,\,\mathrm{cont}}}\,, \tag{3}$$

$$f_{\nu,\,\mathrm{cont}}(\lambda_{\mathrm{EL}}) = f_{\lambda,\,\mathrm{cont}}\,\frac{\lambda_{\mathrm{EL}}^2}{c}\,. \tag{4}$$

For each galaxy in the 5σ line flux-limited sample, we simulate an imaging survey counterpart by extrapolating its continuum flux density from the observed emission line wavelength (λ_{EL}) to a specified broadband imaging survey filter. The power law slope of the continuum is simulated from the distributions of $r'-z'$ colors of LAEs and [O II] emitters observed in the HETDEX Pilot Survey[13] (HPS; Adams et al. 2011; Blanc et al. 2011; Bridge et al. 2015). The procedure prescribed by Madau (1995) is applied to simulated spectra as a function of observed wavelength to correct for absorption by neutral hydrogen in the intergalactic medium (the "Lyα forest"; Lynds 1971). The sum of the resulting flux from the continuum and flux contributed by emission lines, multiplied by the transmission fraction of the specified imaging filter (including the quantum efficiency of the CCD) results in the continuum flux density observed for each galaxy in simulated aperture photometry. One-fifth of the 5σ depth of the simulated imaging survey (SDSS g' and r' filters are assumed in this work; Doi et al. 2010) is used as the standard deviation for the Gaussian profile of measurement noise in photometry.

For each model 5σ emission line detection, we compute a new quantity — *photometric equivalent width* — as the relative strength of the simulated line flux to the continuum flux density measured in aperture photometry. These simulated photometric equivalent widths are observed-frame quantities with measurement noise propagated from both simulated line flux and simulated continuum flux density measurements. As a result of their larger equivalent widths and greater luminosity distances from Earth, among 5σ line detections LAEs are generally fainter than [O II] emitters in their continua, and their measurements therefore suffer from larger fractional uncertainties than continuum measurements of [O II] emitters.

Figure 3 presents the distribution of inferred Lyα equivalent widths ($W_{\mathrm{Ly}\alpha}$) for a 5σ line flux-limited sample of simulated LAEs and corresponding [O II] emitters, plotted against their continuum flux densities ($f_{\nu,\,\mathrm{cont}}$)

[13] A Gaussian fit of the $r'-z'$ colors of LAEs in the HPS sample has mean $\mu=0.11$ and standard deviation $\sigma=0.55$; for [O II] emitters in HPS, a Gaussian fit of $r'-z'$ has $\mu=0.53$ and $\sigma=0.28$.

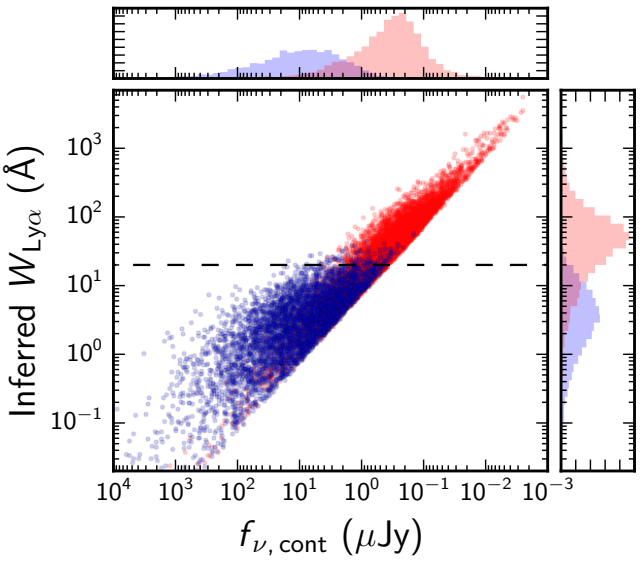

Figure 3. Simulated HETDEX catalog of 1.4×10^6 emission-line galaxies, with g' band imaging ($5\sigma = 25.1$) and realistic measurement noise. Approximately 1 % of the simulated catalog is displayed in the central plot. 842,600 "true" LAEs ($1.9 < z < 3.5$) are shown in red; 538,300 [O II] emitters ($z < 0.48$) are indicated in blue. The horizontal dashed line marks EW = 20 Å in the emission rest frame of Lyα (the traditional selection requirement). The projected histogram along the vertical axis shows the distributions of equivalent widths of the simulated galaxies in the emission rest frame, inferred by assuming each primary line detection is Lyα. The projected histogram along the horizontal axis presents the distributions of continuum density density measured for the galaxies in simulated aperture photometry.

obtained in simulated aperture photometry on g' band imaging with 5σ depth of 25.1 mag. The horizontal dashed line denotes an equivalent width of 20 Å in the rest frame of Lyα emission.

2.2. *Bayesian Classification of Emission-line Galaxies*

HETDEX will use the two-point correlation function, or power spectrum, of high-redshift LAEs to measure dark energy evolution over $1.9 < z < 3.5$ (Hill et al. 2008; Adams et al. 2011). When [O II] emitters are misidentified as LAEs, the correlations of low-redshift galaxies with smaller comoving separations are erroneously mapped to the correlation function of LAEs (Komatsu 2010). The observed power spectrum is given by the weighted average of the LAE power spectrum, P_{LAE}, and the contamination power spectrum:[14]

$$P_{\mathrm{obs}}\left(k_\perp, k_\parallel\right) = \left(1 - f_{[\mathrm{O\,II}]}\right)^2 P_{\mathrm{LAE}}\left(\sqrt{k_\perp^2 + k_\parallel^2}\right) + f_{[\mathrm{O\,II}]}^2 (\alpha^2\beta)\, P_{[\mathrm{O\,II}]}\left(\sqrt{\alpha^2 k_\perp^2 + \beta^2 k_\parallel^2}\right), \quad (5)$$

where $f_{[\mathrm{O\,II}]}$ is the fraction of [O II] emitters in the total LAE sample, i.e.,

$$f_{[\mathrm{O\,II}]} \equiv \frac{\text{number of contaminating [O II] emitters}}{\text{number of galaxies classified as LAEs}}. \quad (6)$$

Improvement in the quality of the LAE sample can be achieved by increasing the completeness of the statistical sample and/or reducing contamination by [O II] emitters relative to the sample obtained by the minimum equivalent width requirement. A Bayesian method takes other observed information into consideration in addition to the equivalent width for each 5σ line detection for the purpose of making a classification. This additional information comprises the wavelength at which the detected emission line is observed (λ_{EL}), the flux measured for the targeted emission line, and the detection (or non-detection) of other emission lines expected to fall within the spectral range of HETDEX if the emission line is [O II].

2.2.1. *Bayes' Theorem and Classification Threshold*

Bayes' theorem gives the posterior probability of a hypothesis or model H given the observed data B:

$$P(H|B) = \frac{P(B|H)P(H)}{P(B)}. \quad (7)$$

For a discrete set of N models, the probability of the data B is simply

$$P(B) = \frac{1}{N}\sum_{j=1}^{N} P(B|H_j). \quad (8)$$

For two competing models H_1 and H_2, the *posterior odds ratio* is

$$\frac{P(H_1|B)}{P(H_2|B)} = \frac{P(H_1)}{P(H_2)}\frac{P(B|H_1)}{P(B|H_2)}, \quad (9)$$

where the first term on the right-hand side is the *prior odds ratio* and the second term, the ratio of the marginal likelihoods under the two models, is called the *Bayes factor* (Gelman et al. 1995; Ivezić et al. 2014). The normalization given by Equation (8) cancels out.

For our application in the present work, in which we seek to classify galaxies detected via a single emission line into two samples, namely, high-redshift LAEs (the target sample) and foreground [O II] emitters (the dominant contaminant), the relevant posterior odds ratio is

$$\frac{P(\mathrm{LAE}|\mathrm{data})}{P\big([\mathrm{O\,II}]|\mathrm{data}\big)} = \frac{P(\mathrm{LAE})}{P\big([\mathrm{O\,II}]\big)}\frac{P(\mathrm{data}|\mathrm{LAE})}{P\big(\mathrm{data}|[\mathrm{O\,II}]\big)}. \quad (10)$$

The natural threshold of the posterior odds ratio to classify an emission-line detection as LAE is >1, but this threshold parameter may be *tuned* to optimize cosmological results, that is, to minimize variance in d_A, our estimator of the two-point correlation function.

2.2.2. *Prior Probabilities and Prior Odds Ratio*

The prior probability that an object is an LAE or an [O II] emitter is calculated as a function of wavelength, using the luminosity functions and cosmological volume elements at the corresponding redshifts. For a given model, an observed emission-line wavelength λ_{EL} corresponds to exactly one redshift z:

$$\lambda_{\mathrm{EL}} = (1+z)\,\lambda, \quad (11)$$

where λ is the line wavelength in the emission rest frame. The assumed cosmology (given in § 1) determines the comoving volume δV_c of each redshift "slice" δz, corre-

[14] See Appendix A for the derivation of Equation (5).

sponding to a wavelength interval $\delta\lambda$ in the observed frame.[15]

Under the simplifying assumption that there are only two types of emission-line objects, the prior probability that a detected line is Lyα and the prior probability that it is [O II] sum up to unity for a given interval $\delta\lambda$:

$$P(\mathrm{LAE}) + P\big([\mathrm{O\,II}]\big) = 1\,. \tag{12}$$

Therefore the prior probability that a detected line is Lyα is the product of the number density at redshift z and the comoving volume at a corresponding redshift interval δz:

$$P(\mathrm{LAE}) = \frac{n_1 \delta V_1}{n_1 \delta V_1 + n_2 \delta V_2}\,. \tag{13}$$

Similarly, the prior probability that a detected line is [O II] is

$$P([\mathrm{O\,II}]) = \frac{n_2 \delta V_2}{n_1 \delta V_1 + n_2 \delta V_2}\,. \tag{14}$$

The integral of the Schechter function (Equation 1) down to the line luminosity corresponding to the flux detection limit yields the number densities:

$$n_1 = \int_{L^{\min}_{\mathrm{LAE}}/L^*_{\mathrm{LAE}}}^{\infty} \phi^*_{\mathrm{LAE}} \left(\tfrac{L}{L^*}\right)^{\alpha_{\mathrm{LAE}}} e^{-L/L^*} d\left(\tfrac{L}{L^*}\right)\,, \tag{15a}$$

$$n_2 = \int_{L^{\min}_{[\mathrm{O\,II}]}/L^*_{[\mathrm{O\,II}]}}^{\infty} \phi^*_{[\mathrm{O\,II}]} \left(\tfrac{L}{L^*}\right)^{\alpha_{[\mathrm{O\,II}]}} e^{-L/L^*} d\left(\tfrac{L}{L^*}\right)\,, \tag{15b}$$

where the vector of parameters $\boldsymbol{\theta} = (\alpha, L^*, \phi^*)$ is described in § 2.1.1 and given in Table 1, and the lower limits of integration are related to the wavelength-dependent flux detection limit $f_{\min}$ as follows:

$$L^{\min}_{\mathrm{LAE}}(\lambda_{\mathrm{EL}}) = 4\pi \left[d_L\big(z_{\mathrm{LAE}}(\lambda_{\mathrm{EL}})\big)\right]^2 f_{\min}(\lambda_{\mathrm{EL}})\,, \tag{16a}$$

$$L^{\min}_{[\mathrm{O\,II}]}(\lambda_{\mathrm{EL}}) = 4\pi \left[d_L\big(z_{[\mathrm{O\,II}]}(\lambda_{\mathrm{EL}})\big)\right]^2 f_{\min}(\lambda_{\mathrm{EL}})\,, \tag{16b}$$

where d_L is luminosity distance. The volume of the interval $z \pm \delta z$ is given by the differential comoving volume integrated over the redshift interval corresponding to $\lambda_{\mathrm{EL}} \pm \delta\lambda$:[16]

$$\delta V_1 = \delta V_c(z_{\mathrm{LAE}}) = \int_{z_{\mathrm{LAE}}-\delta z}^{z_{\mathrm{LAE}}+\delta z} dV_c\,, \tag{17a}$$

$$\delta V_2 = \delta V_c(z_{[\mathrm{O\,II}]}) = \int_{z_{[\mathrm{O\,II}]}-\delta z}^{z_{[\mathrm{O\,II}]}+\delta z} dV_c\,. \tag{17b}$$

The Schechter function integral down to a specified lower limit is the upper incomplete gamma function:

$$\Gamma(s, x) = \int_x^{\infty} t^{s-1}\, e^{-t}\, dt\,. \tag{18}$$

The prior odds ratio is therefore

$$\frac{P(\mathrm{LAE})}{P\big([\mathrm{O\,II}]\big)} = \frac{n_1 \delta V_1}{n_2 \delta V_2}\,. \tag{19}$$

[15] Here, $\delta\lambda$ denotes a fixed interval of λ_{EL} and not the uncertainty of each detected line.

[16] Note that δz, which corresponds to a fixed interval $\delta\lambda$ in the observed frame (Equation 11), has different values under the assumption of each model.

In the case of HETDEX, this assumption of Equation (12) is reasonable. Since the VIRUS spectrographs only extend to 5500 Å, lines such as Hβ and the [O III] doublet will not be observable past $z \sim 0.13$ (see § 3.3). Moreover, while AGN may produce strong line emission at 1549 Å (C IV), 1909 Å (C III]), and 2798 Å (Mg II), the VIRUS coverage is such that these objects will seldom be single-line detections (see § 4.5). By far, the dominant source of confusion is between [O II] and Lyα (Adams et al. 2011).

2.2.3. *Likelihood Functions and Bayes Factor*

The luminosity functions and equivalent width distributions reported by Gronwall et al. (2016) for $z = 2.1$ and $z = 3.1$ populations of LAEs represent the best current information on the properties of LAEs in the HETDEX redshift range. By interpreting these distributions as *probability density functions*, we can calculate the marginal likelihood of measuring the observed data under the assumption that the object is an LAE. The marginal likelihood of the observation given that the observed object is an [O II] emitter is similarly obtained from the galaxy property distributions for [O II] emitters sampled at $0 < z < 0.56$ by Ciardullo et al. (2013). Since any correlation between emission-line luminosity and equivalent width is, at best, weak (Cowie et al. 1996; Hogg et al. 1998; Gronwall et al. 2007; Ciardullo et al. 2012, 2013), we treat these two quantities as statistically independent.

The likelihood function of the observed data B under the assumption of model H_j is

$$P(B|H_j) = \frac{1}{n_j} \int_{a_{j-}}^{a_{j+}} \Phi_j(L)\, dL \int_{b_{j-}}^{b_{j+}} \Psi_j(W)\, dW \tag{20}$$

where n_j is the normalization of the Schechter function integral, $j \in \{1, 2\}$, as given in Equations (15); the luminosity function Φ and the equivalent width distribution Ψ are given in Equations (1) and (2), respectively; and the limits of integration are

$$a_{j\pm} = L_j(f_{\mathrm{EL}}) \pm \delta L_j\,, \tag{21}$$

$$b_{j\pm} = W_j(\mathrm{EW_{obs}}) \pm \delta W_j\,. \tag{22}$$

where δL_j and δW_j denote small fractional changes to the corresponding model quantities, with the fraction of change held fixed across the hypotheses.

The exponential form of the equivalent width distribution $\Psi(W)\, dW$ given in Equation (2) already includes the proper normalization.[17] The luminosity of the emission line is calculated as in Equations (16), but with f_{EL} replacing $f_{\min}$, i.e.,

$$L_{\mathrm{Ly}\alpha}(f_{\mathrm{EL}}, \lambda_{\mathrm{EL}}) = 4\pi \left[d_L\big(z_{\mathrm{LAE}}(\lambda_{\mathrm{EL}})\big)\right]^2 f_{\mathrm{EL}}\,, \tag{23a}$$

$$L_{[\mathrm{O\,II}]}(f_{\mathrm{EL}}, \lambda_{\mathrm{EL}}) = 4\pi \left[d_L\big(z_{[\mathrm{O\,II}]}(\lambda_{\mathrm{EL}})\big)\right]^2 f_{\mathrm{EL}}\,. \tag{23b}$$

The Bayes factor used to calculate the posterior odds

[17] The same is true for the lognormal form to be given in Equation (28) in § 4.1.

ratio given in Equation (10) is

$$\frac{P(\text{data}|\text{LAE})}{P(\text{data}|[\text{O II}])} = \frac{n_2}{n_1} \frac{\int_{L_{\text{Ly}\alpha}-\delta L}^{L_{\text{Ly}\alpha}+\delta L} \Phi_{\text{LAE}}(L)\,dL}{\int_{L_{[\text{O II}]}-\delta L}^{L_{[\text{O II}]}+\delta L} \Phi_{[\text{O II}]}(L)\,dL} \frac{\int_{W_{\text{Ly}\alpha}-\delta W}^{W_{\text{Ly}\alpha}+\delta W} \Psi_{\text{LAE}}(W)\,dW}{\int_{W_{[\text{O II}]}-\delta W}^{W_{[\text{O II}]}+\delta W} \Psi_{[\text{O II}]}(W)\,dW}. \quad (24)$$

The present analysis assumes perfect knowledge of luminosity functions and equivalent width distributions for the simulated populations of targeted LAEs and low-redshift [O II] contaminants. While this is overly optimistic at present, the initial season of HETDEX data will measure the luminosity functions and equivalent width distributions of both populations to high precision. Section 4.1 explores how this assumption affects our results. In practice, HETDEX data will allow for iterative refinement of our Bayesian *priors*, as the luminosity functions and equivalent width distributions of LAEs and [O II] emitters, and their evolution as functions of redshift, become more precisely known.

3. RESULTS

3.1. *Cosmological Distance Measurement Uncertainties*

In order to obtain an indicator of the performance of each classification method, we parametrize the fractional uncertainty in angular diameter distance (d_A) measurements as a function of contamination and incompleteness of the statistical sample of LAEs, as follows:

$$\frac{\sigma_{d_A}}{d_A} = Ax_0^B + Cx_1^D + Ex_0^F x_1^G + H\,, \quad (25)$$

where $x_0 = f_{[\text{O II}]}$ is fractional contamination (as defined in Equation 6) and $x_1 = 1 - N^{\text{true LAEs}}_{\text{recovered}}/N^{\text{true LAEs}}_{\text{available}}$ is sample incompleteness. We use the observable power spectrum (Equation 5) in a Fisher (1935) matrix code[18] (Shoji et al. 2009) that marginalizes over the contamination power spectrum (the second term in Equation 5) to obtain σ_{d_A}/d_A for a grid of contamination and incompleteness values. A linear bias factor of 2.0 is used for LAEs in both redshift bins. We then use the grid of results to derive a fitting formula for the parameters. The value of σ_{d_A}/d_A corresponding to "perfect" classification in each redshift bin ($1.9 < z < 2.5$ and $2.5 < z < 3.5$) is given by the parameter H in Table 2.

Results for Bayesian classification of emission-line galaxies in a simulated HETDEX catalog are presented for an optimized requirement of the posterior odds ratio (Equation 10) for selection as LAEs. This requirement minimizes σ_{d_A}/d_A given perfect information on the simulated object labels by optimizing the trade-off between contamination and incompleteness. Each redshift bin may be optimized independently to maximize the total amount of information obtained from the full $1.9 < z < 3.5$ LAE sample. To accomplish this goal, we need to determine a set of values for the eight parameters in Equation (25) for each redshift bin. In our analysis we divided the full spectral range of HETDEX into two redshift bins and tuned the required posterior odds ratio for LAE classification in each bin separately; Figure 4 and Tables 3 and 4 present results corresponding to a Bayesian method optimized separately for two redshift bins. The value of σ_{d_A}/d_A in total is estimated by inverse variance summation.

[18] http://wwwmpa.mpa-garching.mpg.de/~komatsu/crl/list-of-routines.html

Table 2
Number of observable LAEs in the main HETDEX spring field at nominal flux limits based on `Gr16` Schechter functions, with simulated spectroscopic measurement noise, and the corresponding parameter values for Equation (25) determined by Fisher matrix analysis

Redshift bin	$1.9 < z < 2.5$	$2.5 < z < 3.5$
LAE counts	446,200	396,400
Parameter	Fisher matrix-derived values	
A	3.462	3.758
B	1.323	0.917
C	1.359	3.539
D	1.263	1.803
E	11.65	8.934
F	0.775	1.099
G	3.586	1.085
H	1.409	1.901

3.2. *Improvement over Traditional Equivalent Width Method*

Compared to the traditional $W_{\text{Ly}\alpha} > 20$ Å narrowband limit to classify emission-line galaxies as LAEs (which discards all data below the dashed line in Figure 3), the Bayesian method presented in § 2.2 recovers a more complete statistical sample of high-redshift LAEs without an overall increase in misidentified low-redshift [O II] emitters. Our Bayesian method is adaptive to prior probabilities that reflect the evolution of the galaxy populations and the effect of cosmological volume on the relative density of galaxies as a function of wavelength.

LAEs at $z < 2.065$ are not contaminated by foreground [O II] emitters, since [O II] will not be detected at $\lambda_{\text{EL}} < 3727$ Å. Moreover, at $z < 0.05$, a galaxy's angular scale is greater than 1″ per kpc, hence all but the most compact [O II] sources will be resolved in the imaging survey. Consequently, out to about $z \sim 2.4$, our Bayesian analysis recovers all LAEs with negligible [O II] contamination (see Figure 4, top row).

The rate of contamination in the LAE sample identified by our Bayesian method is sub-percent up to $z \sim 3.0$. Over $1.88 < z < 2.54$, the Bayesian method recovers more than 99% of available LAEs, compared to a sample identified by the traditional $W_{\text{Ly}\alpha} > 20$ Å cutoff that is only ∼ 70% complete.

Table 3 provides a comparative summary of the two classification methods. With respect to the traditional $W_{\text{Ly}\alpha} > 20$ Å cut, the Bayesian method significantly increases the completeness of the sample of objects classified as LAEs by trading near-zero contamination in the case of the EW method for sub-percent contamination in the low-redshift bin ($1.9 < z < 2.5$).

Over the entire HETDEX spectral range (3500–5500 Å), our Bayesian method recovers ∼ 25 % more LAEs than the traditional equivalent width method. Over the redshift range $2 < z < 3$, 86 % of "true" LAEs

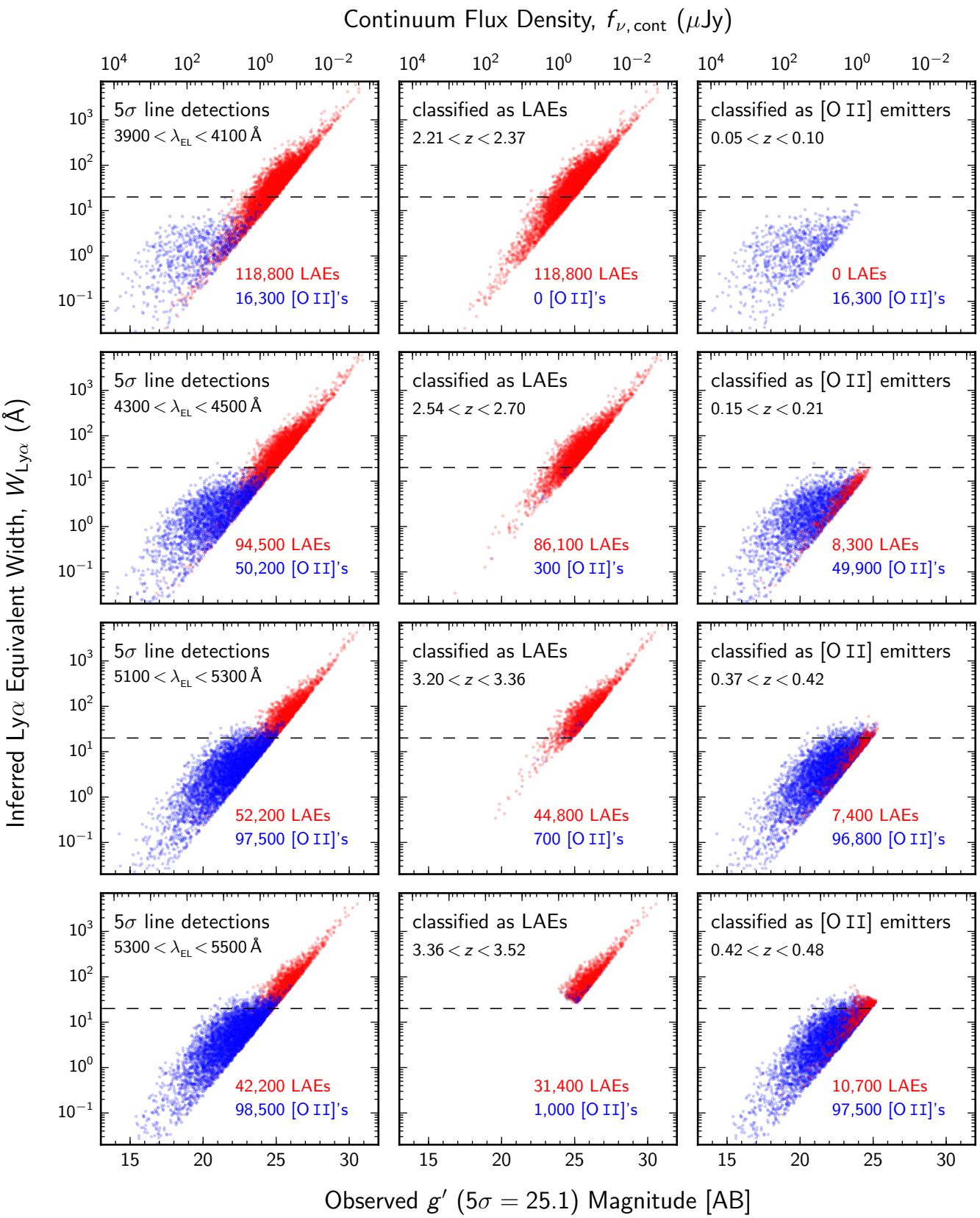

Figure 4. Four selected redshift bins shown in rows for a simulated HETDEX survey with g' ($5\sigma = 25.1$) band imaging survey and realistic measurement noise. Approximately 5 % of the galaxies in each redshift bin are plotted. *Left*: All 5σ spectroscopic detections of emission-line galaxies whose primary lines are observed in the given wavelength interval. *Middle* (*Right*): Simulated emission-line galaxies classified by Bayesian method into high-redshift LAE (foreground [O II]) samples at the corresponding redshifts. Correctly classified "true" LAEs ([O II] emitters) are shown in red (blue); misidentified [O II] emitters (erroneously discarded LAEs) are indicated in blue (red).

Table 3
Classification results for a simulated HETDEX catalog based on `Gr16` luminosity functions and equivalent width distributions, with simulated aperture photometry on g' ($5\sigma = 25.1$) band imaging

Classification method	$W_{\mathrm{Ly}\alpha} > 20$ Å	Bayesian method	
		default [a]	optimized [b]
Galaxies classified as LAEs	637,400	847,500	796,200
Missed observable LAEs	218,700	20,100	50,800
Sample incompleteness	26.0 %	2.39 %	6.02 %
Misidentified [O II] emitters	13,500	25,100	4,400
Fractional contamination	2.12 %	2.96 %	0.55 %
Measurement uncertainty, σ_{d_A}/d_A	1.32 %	1.19 %	1.16 %

[a] The "default" Bayesian requirement for LAE classification is $\frac{P(\mathrm{LAE}|\mathrm{data})}{P([\mathrm{O\,II}]|\mathrm{data})} > 1$.

[b] The "optimized" Bayesian method requires $\frac{P(\mathrm{LAE}|\mathrm{data})}{P([\mathrm{O\,II}]|\mathrm{data})} > 1.38$ for the classification of $1.9 < z < 2.5$ LAEs and $\frac{P(\mathrm{LAE}|\mathrm{data})}{P([\mathrm{O\,II}]|\mathrm{data})} > 10.3$ for $2.5 < z < 3.5$ LAEs.

Table 4
Bayesian method classification results for three simulated HETDEX catalogs with g' band imaging ($5\sigma = 25.1$); "baseline" distributions are used as Bayesian *priors* for each simulation scenario

Simulation scenario	baseline	pessimistic	optimistic
Distribution of LAEs	`Gr16` evolving	`Ci12`, $z = 2.1$ no evolution	`Gr07`, $z = 3.1$ no evolution
Distribution of [O II] emitters	`Ci13`	$+1\sigma\{\phi^*, L^*, w_0\}_{\mathtt{Ci13}}$	$-1\sigma\{\phi^*, L^*, w_0\}_{\mathtt{Ci13}}$
"True" observable LAEs	842,600	375,000	1,155,000
Galaxies classified as LAEs	796,200	345,000	1,075,800
Missed observable LAEs	50,800	32,700	83,500
Sample incompleteness	6.02 %	8.73 %	7.23 %
Misidentified [O II] emitters	4,420	7,700	4,350
Fractional contamination	0.55 %	2.20 %	0.40 %

missed by $W_{\mathrm{Ly}\alpha} > 20$ Å are correctly classified by the Bayesian method, representing the recovery of cosmological information that would be discarded by the equivalent width method. In addition to improving the completeness of the LAE sample, the Bayesian method also reduces contamination by [O II] sources by a factor of ~ 4 in our simulations.

3.3. *Aperture Spectroscopy for Additional Emission Lines*

The presence of other emission lines redward of the primary detected line (in the case of [O II] emitters; see Figure 1), when they fall within the spectral range of HETDEX, provides additional observed information for the two likelihood functions in Equation (24). Accounting for this spectral information leads to better classification performance by the Bayesian method in the form of additional reductions in fractional contamination and further increases in the completeness of the LAE sample.

At $z < 0.1$, the vast majority of [O II]-emitting galaxies will be detected via multiple emission lines; we typically observe stronger [O III] λ5007 emission than [O II] λ3727. For the bulk of the HETDEX [O II] redshift range, $0.13 < z < 0.42$, [Ne III] λ3869 is the only other line that falls into the spectrograph's bandpass.

With our previous assumption of statistically independent quantities, the likelihood functions $P\,(\mathrm{data}|\mathrm{LAE})$ and $P\big(\mathrm{data}|[\mathrm{O\,II}]\big)$ are each the product of the likelihood functions associated with the individual properties we wish to consider:

$$P\,(\mathrm{data}|\mathrm{type}) = \prod_{\mathrm{properties}} P\,(\mathrm{data}|\mathrm{type})_{\mathrm{property}}\ . \quad (26)$$

In particular,

$$P\,(\mathrm{data}|\mathrm{type})_{\mathrm{lines}} = \prod_{\mathrm{lines}} P\,(\mathrm{data}|\mathrm{type})_{\mathrm{line}}\ , \quad (27)$$

where the lines we wish to consider are [Ne III] λ3869, Hβ λ4861, [O III] λ4959, and [O III] λ5007, subject to their falling within the HETDEX spectral range. Assuming a Gaussian noise distribution, we can calculate the probability of the measured flux at each expected line location. When a line is out of range, it contributes no information for or against the hypothesis that the primary detected line is [O II]; the $P\,(\mathrm{data}|\mathrm{type})_{\mathrm{line}}$ in question is set equal to unity, thereby having no effect on the value in the left-hand side of Equation (27).

The improvement due to accounting for additional emission lines is evident when we consider the boundary at which spectroscopic information from all additional lines is lost, when [Ne III] λ3869 is redshifted out of the HETDEX spectral range (3500–5500 Å) for $z > 0.42$ [O II] emitters ($\lambda_{\mathrm{EL}} > 5299$ Å). The bottom row in Figure 4 shows 5σ emission line detections at $5300 < \lambda_{\mathrm{EL}} < 5500$ Å and their classification into samples of LAEs and [O II] emitters. Without spectroscopic information from the additional lines, the Bayesian cutoff between LAEs and [O II] emitters is reduced to a nearly straight line on a log-log plot of $W_{\mathrm{Ly}\alpha}$ versus continuum flux densities ($f_{\nu,\,\mathrm{cont}}$) in this redshift bin, which is the reddest 200 Å in the spectral range of HETDEX (cf. third row in Figure 4).

3.4. *Optimizing Area versus Depth in Fixed Observing Time*

Using our Bayesian method and HETDEX as a baseline scenario, we investigate the survey design trade-off between total survey area and depth of coverage per unit survey area. Holding the amount of available observing time fixed at the HETDEX survey design (denoted by the grey dashed line in Figure 5), we apply 5σ depths in both simulated spectroscopic and imaging surveys that are modified by $1/\sqrt{t}$, where t is the factor by which observing time per unit survey area changes as a result of a corresponding change in total survey area. Simulated measurement noise varies accordingly, as described in § 2.1.

The number of LAEs available to be recovered in the 5σ line flux-limited sample changes with survey design, as shown in the upper panel of Figure 5. For each survey design, we re-run the Fisher matrix code described in § 3.1 with the number of available LAEs to determine a new set of parameters for Equation (25) (i.e., Table 2) and re-optimize the Bayesian method for each case.

Our analysis indicates that the current HETDEX survey design is effectively optimal in the trade-off between area and depth when our Bayesian method is used as the redshift classifier: Trading away from the nominal 300 deg^2 survey area moves the optimal σ_{d_A}/d_A for the two redshift bins in opposite directions (lower panel in Figure 5).

4. DISCUSSION

4.1. *Imperfect Knowledge of Distribution Functions of Galaxy Properties*

The luminosity functions and equivalent width distributions measured by Ciardullo et al. (2013) and Gronwall et al. (2016) represent the best current information on the galaxy populations HETDEX will observe, but will be superseded by data collected in the initial season of HETDEX observations. The ability of the Bayesian method to classify spectroscopic emission-line detections does not crucially depend on perfect knowledge of the characteristics of the galaxy populations. To demonstrate this behavior, we test our method with simulated populations of LAEs with varying characteristics, including cases in which the luminosity function and equivalent width distribution do not evolve with redshift. For these tests, the population of foreground [O II] emitters is simulated as described in § 2.1; the Bayesian method assumes the *priors* given in § 2.2 and uses the LAE classification cutoff optimized for the "baseline" scenario (Table 3). Table 4 compares two such test cases with the "baseline" scenario.

The $z = 3.1$ Lyα luminosity function measured by Gronwall et al. (2007), if assumed to be constant with redshift and applied to the entire redshift range ($1.9 < z < 3.5$), implies more observable LAEs (whose emission-line fluxes exceed the detection limit) at both low and high redshift (see upper-left panel of Figure 2). This result leads to a lower rate of contamination in the LAE sample classified by a Bayesian method that uses the same priors as the baseline and which is optimized with respect to the baseline scenario. Although the Bayesian method recovers a larger LAE sample in this scenario, the sample is more incomplete in fractional

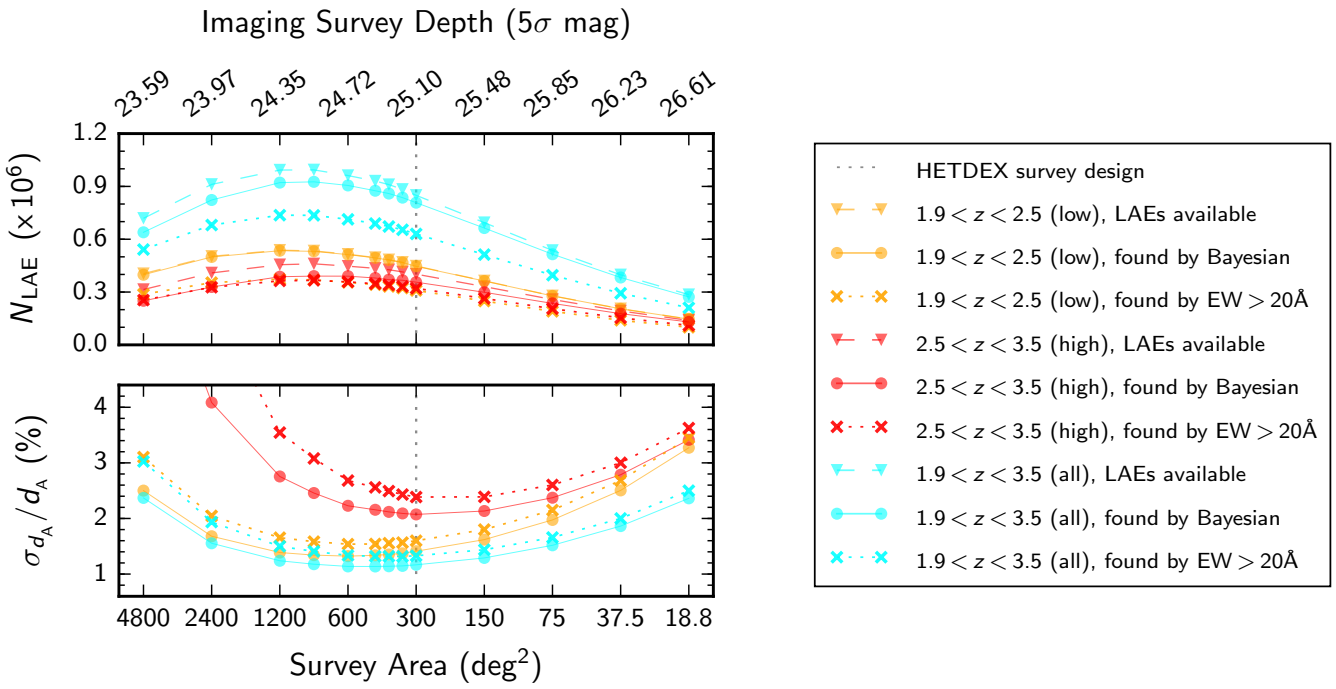

Figure 5. Trade-off between survey area and depth in simulated surveys for $1.9 < z < 3.5$ LAEs in fixed broadband imaging and spectroscopic time. A survey that reaches 25.1 magnitude will cover 300 deg^2. *Top*: Number of LAEs available to be recovered in each simulated survey and numbers correctly identified by each method for LAE classification. *Bottom*: Measurement uncertainty in angular diameter distance (d_A) corresponding to each combination of classification method and redshift range in simulations. The most accurate measurement of d_A occurs with a survey area of 300–600 deg^2.

terms due to the large number of "true" observable LAEs available to be recovered.

The $z = 2.1$ Lyα luminosity function measured by Ciardullo et al. (2012), if assumed to be constant with redshift and applied to the entire redshift range, represents a scenario that is unfavorable for LAE-based cosmological study at high redshift. Nevertheless, our Bayesian method misses fewer observable LAEs and misidentifies fewer [O II] emitters than does the EW method in the baseline scenario.

Blanton & Lin (2000) and Yan et al. (2006) demonstrate that the [O II] equivalent width distribution is also well-fit by a lognormal function. For simulations in which the equivalent widths of [O II] emitters are lognormally distributed, i.e.,

$$\Psi(W)\,dW = \frac{1}{\sqrt{2\pi}\sigma_W}\,\frac{dW}{W}\,\exp\left[-\frac{1}{2\sigma_W^2}\left(\ln\frac{W}{W_0} - \frac{\sigma_W^2}{2}\right)^2\right], \tag{28}$$

our Bayesian method recovers similarly robust LAE samples assuming either exponential or lognormal distributions as priors. For this test, we fit the `Ci13` exponential distributions to the form of Equation (28) for $W > 5$ Å. These lognormal fits are shown in the lower-right panel of Figure 2; the fitted parameters are presented in the far-right column of Table 1.

By accounting for each detected emission line's wavelength, flux, equivalent width, and, in the case of most [O II] emitters ($z < 0.42$), additional lines present in the galaxy spectrum, the Bayesian method's overall ability to identify high-redshift LAEs targeted by HETDEX for cosmological study is only mildly affected by a mismatch between the expected and actual distributions of galaxy properties. This reflects a practical situation in which we do not know the luminosity functions of the "real" populations with high precision at the onset of the survey.

4.2. *Sensitivity to Imaging Survey Depth*

Since the vast majority of [O II] emitters are brighter in their continua than the imaging depth in the survey design of HETDEX, the Bayesian method is able to keep contamination in the sample of objects classified as LAEs under 1 %, down to survey depth AB ∼ 22 mag for the low-redshift bin ($1.9 < z < 2.5$) and AB ∼ 24 mag for the high-redshift bin ($2.5 < z < 3.5$).

Figure 6 demonstrates that for the 3500–4300 Å portion of the HETDEX spectral range (top panel), essentially all observed [O II] emitters have continuum flux densities greater than the 5σ limit of HETDEX broadband imaging, resulting in small equivalent widths and enabling the success of the traditional method for LAE selection in this regime of observed emission line wavelengths. The inclusion of emission line flux in addition to equivalent width in Bayesian classification leads to an LAE sample with a rate of contamination less than a quarter percent.

In the longer wavelength bin (4300–5500 Å, bottom panel of Figure 6), line fluxes measured for [O II] emitters are weaker than those in the shorter-wavelength bin due to increasing luminosity distance, rendering [O II] equivalent widths measured in this bin similar to those of high-redshift LAEs. In this redshift range, accurate classification is relatively difficult for both methods. Equivalent width alone is not an adequate classifier; the inclusion of line flux and information from additional lines enables

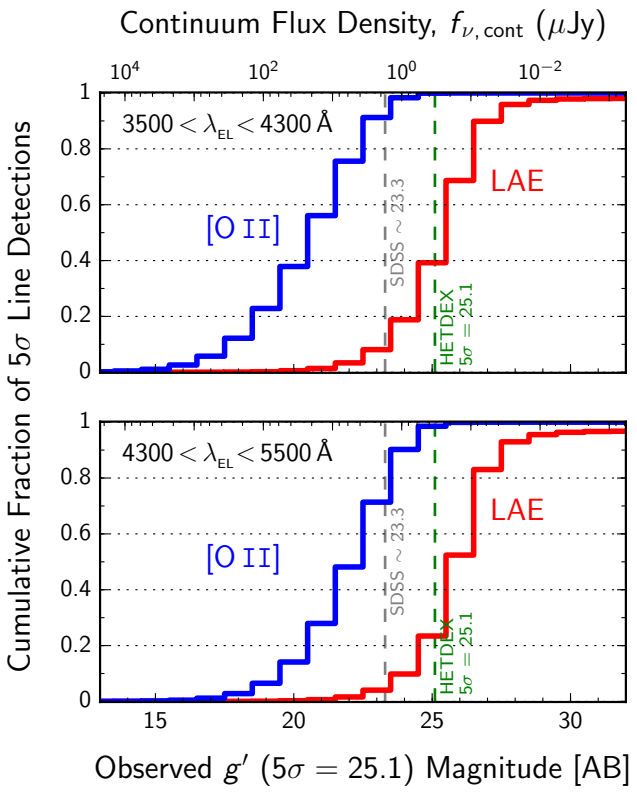

Figure 6. Fractions of 5σ spectroscopic detections of LAEs and [O II] emitters, in a simulated HETDEX survey, brighter than the given observed continuum magnitude of the objects in aperture photometry on simulated g' band imaging.

Bayesian classification to be effective in a regime that poses serious challenges to the traditional $W_{\mathrm{Ly}\alpha} > 20$ Å method.

4.3. *Single Broadband Filter with Best Performance*

The performance of our Bayesian method is similar with g' and r' band simulated imaging in equal observing time, assuming a typical 0.3-mag reduction in equal-time depth going from g' to r'. With the Bayesian method, the improvement in changing from g' ($5\sigma = 25.1$) to r' ($5\sigma = 24.8$) band imaging is a $\sim 1\,\%$ reduction in σ_{d_A}. To place this improvement in perspective, changing from g' to r' with the equivalent width method reduces σ_{d_A}/d_A by $\sim 1.5\,\%$, i.e., the observed distributions of LAEs and [O II] emitters are less similar in r' band imaging. Figure 7 compares simulated g' and r' band imaging for a single realization of a simulated spectroscopic survey.

At higher redshifts ($2.5 < z < 3.5$), suppressing contamination in g' band is problematic for $W_{\mathrm{Ly}\alpha} > 20$ Å. The relatively red colors of [O II] emitters (Bridge et al. 2015) lead to weaker continuum flux density measurements in the g' band, leading to larger photometric equivalent widths for [O II] determined by aperture photometry on g' band imaging (Equation 3). This results in a higher rate of contamination in the LAE sample selected by the traditional EW method versus the case of r' band imaging. In contrast, our Bayesian method is able to optimize its requirement for LAE classification given the selection of a broadband filter.

4.4. *Splitting Available Observing Time to Obtain Color*

Inclusion of the colors of galaxies as additional input to the Bayesian method results in modest further reductions in measurement uncertainty in angular diameter distance. In $2.5 < z < 3.5$, splitting available observing time between g' and r' in our simulations and using the distributions of $g'-r'$ colors of LAEs and [O II] emitters found by HPS (Bridge et al. 2015) as additional Bayesian *priors* result in $\sim 5\,\%$ improvement in σ_{d_A}/d_A over devoting all available observing time to obtaining g' band imaging in full (25.1 mag) depth. Tests of other broadband filter combinations yield similar results.

4.5. *Other Sources of Contamination*

Each of the "additional" emission lines in [O II] spectra targeted for aperture spectroscopy (§ 3.3) may in fact be a 5σ line detection in its own right. However, detections of Hβ λ4861, [O III] λ4959, and/or [O III] λ5007 nearly guarantee that [O II] λ3727 will also be detected within the HETDEX spectral range. Therefore, [O III] will not be a significant source of contamination (Adams et al. 2011).

AGNs represent another potential source of confusion for identifying LAEs. In most cases, detection of strong C IV λ1549 provides an indication of the source's nature; C IV shifts into the HETDEX spectral range at $z = 1.25$. C III] λ1909 shifts out of the red-end of the HETDEX range at $z = 1.88$, but not before Lyα λ1216 shifts into range at the blue-end of HETDEX. Hence when C IV is observed, we always expect to detect C III] or Lyα.

Spurious emission line detections caused by cosmic rays represent a significant source of contamination. Our Bayesian method can be broadened to account for these spectroscopic detections that have no counterpart in the imaging survey; doing so will greatly increase the importance of deep imaging.

4.6. *Application to Future Surveys*

4.6.1. *Narrowband Surveys*

In our application (HETDEX), continuum emission is not well measured in spectroscopy for emission line-selected objects, necessitating a complementary broadband imaging survey for redshift classification of targeted objects. In addition to spectroscopic emission line surveys, the Bayesian method presented in this work is equally applicable to narrowband surveys.

There are two limiting cases. In the first, where the narrowband filters have top-hat transmission profiles (e.g., Ciardullo et al. 2012), each object's line flux will be well-determined, while the precision of its redshift measurement is limited to the width of the filter. In the second case, the filter transmission curves may be Gaussian (e.g., Gronwall et al. 2007). In this scenario, there is an additional probability associated with the location of the emission line within the filter bandpass, which creates uncertainty in converting narrowband flux density excess into an equivalent width. In either case, ancillary broadband data are required to determine the equivalent widths of detected emission lines. Redshift classifications can then be made to identify galaxies targeted by the survey.

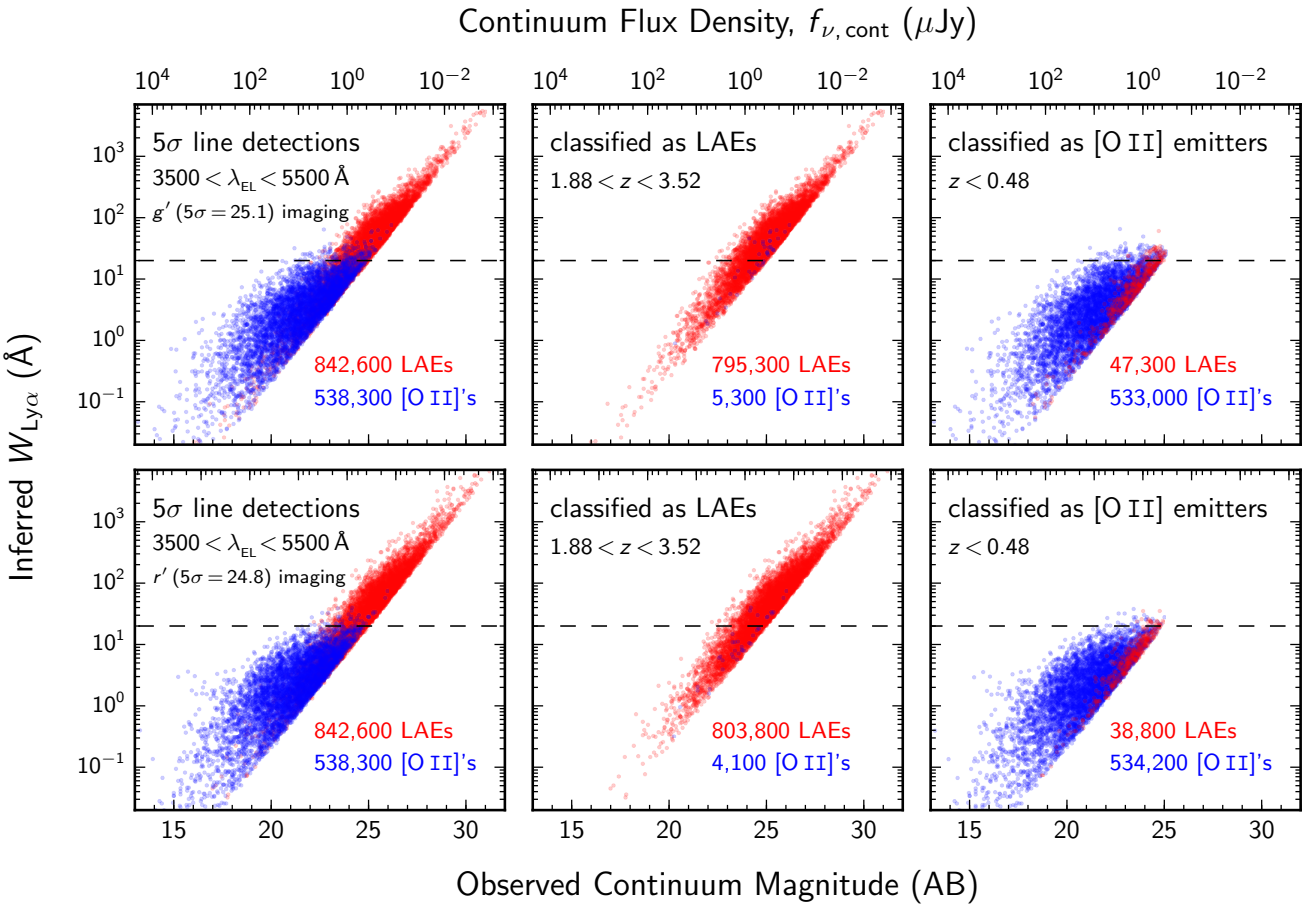

Figure 7. Classification results for a simulated spectroscopic survey coupled with g' band imaging (*top*) and r' band imaging (*bottom*). Approximately 1 % of each simulated catalog is plotted. The distributions of Lyα and [O II] equivalent widths are less similar in simulated r' band imaging, resulting in a moderate improvement in classification with respect to the case of g' band imaging.

4.6.2. *Euclid and WFIRST*

Future surveys by the *Euclid* space mission and the space-based Wide-Field Infrared Survey Telescope (WFIRST) will conduct cosmological studies via BAO measurements with slitless spectroscopy for Hα emission-line galaxies at $0.7 < z < 2.1$ (Laureijs et al. 2011) and $1.3 < z < 2.7$ (Green et al. 2012), respectively. Due to their nature in targeting a specific line for detection, these types of investigations are generally susceptible to contamination by other strong line emissions. For example, Geach et al. (2008, 2010) have found that [O III] λ5007, Paα, Paβ, and [Fe II] may all be confused with Hα in low-resolution surveys.

A similar Bayesian method can assist these projects, which will have many broadbands available. For application to these upcoming experiments, the method should be broadened to include photometric redshift probabilities in addition to the luminosity functions and equivalent width distributions considered in this study.

When broadband photometric redshifts are available (Pullen et al. 2015), they can be combined with our EW-based probabilities to yield a more robust classification, via $R_{\mathrm{total}} = R_{\mathrm{photo}\text{-}z} \times R_{\mathrm{EW}}$, where R refers to posterior odds ratios of LAE versus [O II]. However, these quantities share the information of the continuum flux density near the emission-line wavelength, so they are not completely independent, and hence it would be preferable to perform a joint analysis such as template-fitting including emission-line information.

4.7. *Use of Classification Probabilities in Large-scale Structure Analyses*

The parametrization of σ_{d_A}/d_A given by Equation (25) implicitly assumes that d_A is produced by way of the power spectrum calculated from point estimates of redshift (correspondingly, of object label) based on a cut in classification probability. If we instead consider the catalog to comprise observed objects each with a known classification probability, we may retain potentially valuable information in calculating summary statistics for both populations.

Instead of reducing a probabilistic catalog to a traditional classification problem, we may do hierarchical inference directly on the classification probabilities to obtain the contamination fraction necessary for calculation of the power spectrum, as outlined in Appendix A (Malz & Hogg 2016, in prep). An alternative and more ambitious approach would convert the classification probabilities to redshift probabilities, thereby replacing the density field necessary for the calculation of the power

spectrum with one that treats each object as having a probability distribution over redshift, a sum of components proportional to the classification probabilities at the redshifts corresponding to the galaxy types in question. Both of these approaches would preserve the knowledge of the classification probabilities but would require greater computational cost, as the calculation of the two-point correlation function must take more information into account.

5. CONCLUSIONS

The Bayesian method presented in this work for the classification of LAEs offers robust improvements over the traditional limit requiring LAEs to have rest-frame equivalent width ($W_{\mathrm{Ly}\alpha}$) greater than 20 Å. The statistical discriminating power of our Bayesian method derives from cosmological volumes of the corresponding redshifts based on the assumed cosmology, the properties measured for previously observed samples of LAEs and [O II] emitters, and known positions of other emission lines in the spectra of [O II] emitters. For a simulated HETDEX catalog with realistic measurement noise, our Bayesian method:

- Recovers 86 % of LAEs missed by the $W_{\mathrm{Ly}\alpha} > 20$ Å cutoff over $2 < z < 3$;
- Outperforms $W_{\mathrm{Ly}\alpha} > 20$ Å in limiting contamination in the LAE sample and increases the completeness of the statistical sample;
- Allows trade-off between contamination and incompleteness in arbitrary wavelength/redshift bins.

For simulated HETDEX catalogs, Table 3 shows that our implementation of the Bayesian method reduces uncertainties in angular diameter distance measurements by 14 %, which is equivalent to obtaining 29 % more data, compared to the $W_{\mathrm{Ly}\alpha} > 20$ Å criterion.

Additional conclusions of our investigation are:

- For fixed spectroscopic depths, performance of the Bayesian method is relatively insensitive to imaging survey depth, suggesting that maximizing imaging survey area should be favored in a fixed amount of observing time for the purpose of LAE-[O II] galaxy separation;
- Inclusion of the colors of galaxies as an input to the Bayesian method increases discriminating power and results in modest further reductions in distance errors;
- The Bayesian method can also be used to determine which single broadband filter produces the best performance;
- The Bayesian method can be directly applied to other surveys where single emission lines require classification, including planned space-based observations by *Euclid* and WFIRST.

Unlike the Bayesian approach, machine learning methods do not require prior assumptions on the luminosity functions and equivalent width distributions of galaxies, but they require a sizable training set, consisting of ancillary data for which the object labels are known for 5 to 10 % of the survey (Acquaviva et al. 2014). As a result, we anticipate the combination of these two complementary classification approaches to yield additional improvements.

We thank the referee for providing critical comments and detailed suggestions, which have led to substantial improvement in the clarity of the method presented in this paper. E. G. and A. S. L. gratefully acknowledge support from the NSF through Grant AST-1055919. E. K. is supported in part by MEXT KAKENHI Grant Number 15H05896. J. J. F. thanks the University of Texas at Austin for hospitality and support during a sabbatical visit, where a portion of this work was completed.

REFERENCES

Acquaviva, V., Gawiser, E., Leung, A. S., & Martin, M. R. 2014, in Proceedings of the IAU Symposium, Vol. 306, Statistical Challenges in 21st Century Cosmology, ed. A. Heavens, J.-L. Starck, & A. Krone-Martins (Lisbon, Portugal: IAU), 81
Adams, J. J., Blanc, G. A., Hill, G. J., et al. 2011, ApJS, 192, 5
Anders, P., & Fritze-v. Alvensleben, U. 2003, A&A, 401, 1063
Blake, C., & Glazebrook, K. 2003, ApJ, 594, 665
Blanc, G. A., Adams, J. J., Gebhardt, K., et al. 2011, ApJ, 736, 31
Blanton, M., & Lin, H. 2000, ApJ, 543, L125
Bridge, J. S., Gronwall, C., Ciardullo, R., et al. 2015, ApJ, 799, 205
Ciardullo, R., Gronwall, C., Wolf, C., et al. 2012, ApJ, 744, 110
Ciardullo, R., Gronwall, C., Adams, J. J., et al. 2013, ApJ, 769, 83
Comparat, J., Richard, J., Kneib, J.-P., et al. 2015, A&A, 575, A40
Cowie, L. L., & Hu, E. M. 1998, AJ, 115, 1319
Cowie, L. L., Songaila, A., Hu, E. M., & Cohen, J. G. 1996, AJ, 112, 839
Doi, M., Tanaka, M., Fukugita, M., et al. 2010, AJ, 139, 1628
Fisher, R. A. 1935, Journal of the Royal Statistical Society, 39
Gallego, J., García-Dabó, C. E., Zamorano, J., Aragón-Salamanca, A., & Rego, M. 2002, ApJ, 570, L1
Gallego, J., Zamorano, J., Rego, M., Alonso, O., & Vitores, A. G. 1996, A&AS, 120, 323
Gawiser, E., van Dokkum, P. G., Gronwall, C., et al. 2006, ApJ, 642, L13
Geach, J. E., Smail, I., Best, P. N., et al. 2008, MNRAS, 388, 1473
Geach, J. E., Cimatti, A., Percival, W., et al. 2010, MNRAS, 402, 1330
Gelman, A., Carlin, J. B., Stern, H. S., & Rubin, D. B. 1995, Bayesian Data Analysis (Boca Raton, FL: CRC Press)
Green, J., Schechter, P., Baltay, C., et al. 2012, ArXiv e-prints, arXiv:1208.4012
Gronwall, C., Ciardullo, R., Hickey, T., et al. 2007, ApJ, 667, 79
Gronwall, C., Ciardullo, R., Matković, A., et al. 2016, in preparation
Guaita, L., Gawiser, E., Padilla, N., et al. 2010, ApJ, 714, 255
Henry, A. L., Martin, C. L., Dressler, A., Sawicki, M., & McCarthy, P. 2012, ApJ, 744, 149
Hill, G. J., & HETDEX Collaboration. 2015, in Multi-object Spectroscopy in the Next Decade: Big Questions, Large Surveys and Wide Fields, ed. I. Skillen, S. C. Trager, M. Balcells, & C. Benn (Santa Cruz de La Palma, Canary Islands, Spain: ASP), Astronomical Society of the Pacific Conference Series
Hill, G. J., Gebhardt, K., Komatsu, E., et al. 2008, in Astronomical Society of the Pacific Conference Series, Vol. 399, Panoramic Views of Galaxy Formation and Evolution, ed. T. Kodama, T. Yamada, & K. Aoki (Hayama, Japan: ASP), 115
Hippelein, H., Maier, C., Meisenheimer, K., et al. 2003, A&A, 402, 65
Hogg, D. W., Cohen, J. G., Blandford, R., & Pahre, M. A. 1998, ApJ, 504, 622

Hu, W., & Haiman, Z. 2003, Phys. Rev. D, 68, 063004
Ivezić, Ž., Connelly, A. J., VanderPlas, J. T., & Gray, A. 2014, Statistics, Data Mining, and Machine Learning in Astronomy (Princeton, NJ: Princeton University Press)
Koehler, R. S., Schuecker, P., & Gebhardt, K. 2007, A&A, 462, 7
Komatsu, E. 2010, HETDEX Collaboration memo. "Note on the effect of [O II] emitters"
Komatsu, E., Smith, K. M., Dunkley, J., et al. 2011, ApJS, 192, 18
Laureijs, R., Amiaux, J., Arduini, S., et al. 2011, ArXiv e-prints, arXiv:1110.3193
Ly, C., Malkan, M. A., Kashikawa, N., et al. 2007, ApJ, 657, 738
Lynds, R. 1971, ApJ, 164, L73
Madau, P. 1995, ApJ, 441, 18
Malz, A. I., & Hogg, D. W. 2016, in preparation
Oke, J. B., & Gunn, J. E. 1983, ApJ, 266, 713
Osterbrock, D. E. 1974, Astrophysics of Gaseous Nebulae (San Francisco, CA: W. H. Freeman and Co.)
Ouchi, M., Shimasaku, K., Akiyama, M., et al. 2008, ApJS, 176, 301
Planck Collaboration, Ade, P. A. R., Aghanim, N., et al. 2015, ArXiv e-prints, arXiv:1502.01589
Pullen, A. R., Hirata, C. M., Dore, O., & Raccanelli, A. 2015, ArXiv e-prints, arXiv:1507.05092
Schechter, P. 1976, ApJ, 203, 297
Seo, H.-J., & Eisenstein, D. J. 2003, ApJ, 598, 720
—. 2007, ApJ, 665, 14
Shimasaku, K., Kashikawa, N., Doi, M., et al. 2006, PASJ, 58, 313
Shoji, M., Jeong, D., & Komatsu, E. 2009, ApJ, 693, 1404
Takahashi, M. I., Shioya, Y., Taniguchi, Y., et al. 2007, ApJS, 172, 456
Teplitz, H. I., Collins, N. R., Gardner, J. P., Hill, R. S., & Rhodes, J. 2003, ApJ, 589, 704
Yan, R., Newman, J. A., Faber, S. M., et al. 2006, ApJ, 648, 281

APPENDIX

A. THE EFFECT OF CONTAMINATION BY [O II] EMITTERS

When [O II] λ3727 lines are misidentified as Lyα λ1216 lines, we erroneously map the correlation function of [O II] galaxies at low redshifts to the correlation function of LAEs at high redshifts. As a result, instead of measuring the correlation at some comoving separations between LAEs at $z>1.9$, we actually measure the correlation of [O II] emitters at smaller comoving separations at $z<0.5$.

This effect can be formulated most straightforwardly using real space correlation functions. Let us imagine that, from the HETDEX data, we measured the correlation function, $\xi(\boldsymbol{\theta} d_A, s_\parallel)$, where $\boldsymbol{\theta}$ is the angular separation on the sky, d_A is the comoving angular diameter distance to a given redshift (assigned to LAEs, including misidentified [O II] emitters), and $s_\parallel$ is the line-of-sight separation.

A problem arises because since we misidentified the [O II] lines for Lyα lines, our assumed values of d_A and $s_\parallel$ are incorrect.

Let us denote the correlation function of the contamination at $z>1.9$ as $\xi_{\rm con}$, and the true correlation function of the [O II] emitters at $z<0.5$ as $\xi_{\rm [O\,II]}$. As these are the same objects, except for the values of the spatial coordinates assigned to each, we have a trivial relation:

$$\xi_{\rm con}\left(\boldsymbol{\theta} d_A, s_\parallel\right) \,=\, \xi_{\rm [O\,II]}\left(\boldsymbol{\theta} d_A^{\rm [O\,II]}, s_\parallel^{\rm [O\,II]}\right). \tag{A1}$$

The angular separation, $\boldsymbol{\theta}$, is the same for both $\xi_{\rm con}$ and $\xi_{\rm [O\,II]}$. The misidentification of the lines simply produces incorrect values for d_A and $s_\parallel$ on the left-hand side.

The power spectrum can be obtained from the correlation function via the usual inverse Fourier transform:

$$P_{\rm con}\left(\boldsymbol{k}_\perp, k_\parallel\right) = \int d^2\boldsymbol{s}_\perp\, e^{-i\boldsymbol{k}_\perp\boldsymbol{s}_\perp} \int ds_\parallel\, e^{-ik_\parallel s_\parallel}\, \xi_{\rm con}\left(\boldsymbol{s}_\perp, s_\parallel\right), \tag{A2}$$

where $\boldsymbol{s}_\perp \equiv \boldsymbol{\theta} d_A$. We also Fourier transform $\xi_{\rm con}\left(\boldsymbol{s}_\perp, s_\parallel\right)$:

$$\xi_{\rm con}\left(\boldsymbol{s}_\perp, s_\parallel\right) = \xi_{\rm [O\,II]}\left(\boldsymbol{s}_\perp^{\rm [O\,II]}, s_\parallel^{\rm [O\,II]}\right) = \int \frac{d^2\boldsymbol{k}_\perp^{\rm [O\,II]}}{(2\pi)^2}\, e^{i\boldsymbol{k}_\perp^{\rm [O\,II]}\boldsymbol{s}_\perp^{\rm [O\,II]}} \int \frac{dk_\parallel^{\rm [O\,II]}}{2\pi}\, e^{ik_\parallel^{\rm [O\,II]} s_\parallel^{\rm [O\,II]}}\, P_{\rm [O\,II]}\left(k^{\rm [O\,II]}\right). \tag{A3}$$

Now, define the key parameters, the ratios of $s_\perp$ and $s_\parallel$, as follows:

$$\alpha \equiv \frac{s_\perp}{s_\perp^{\rm [O\,II]}} = \frac{d_A}{d_A^{\rm [O\,II]}} > 1, \tag{A4}$$

$$\beta \equiv \frac{s_\parallel}{s_\parallel^{\rm [O\,II]}} = \frac{(1+z)/H(z)}{(1+z_{\rm [O\,II]})/H(z_{\rm [O\,II]})} = \frac{3727}{1216}\frac{H(z_{\rm [O\,II]})}{H(z)} = \frac{3727}{1216}\sqrt{\frac{\Omega_m(1+z_{\rm [O\,II]})^3+\Omega_\Lambda}{\Omega_m(1+z)^3+\Omega_\Lambda}}. \tag{A5}$$

The quantity α is always larger than 1 (i.e., the redshift of LAEs is always higher than that of [O II] emitters), while β can be larger or smaller than 1. Of course, $1+z_{\rm [O\,II]}$ satisfies the relation:

$$1+z_{\rm [O\,II]} = (1+z)\,\frac{1216}{3727} \simeq \frac{1+z}{3.065}. \tag{A6}$$

In Table 5, we summarize the values of α and β for representative redshifts: $z=2.2$ and 3.0.

Table 5
Values of α and β

z	$z_{[\mathrm{O\,II}]}$	$d_A(z)$ [a]	$d_A(z_{[\mathrm{O\,II}]})$ [a]	α [b]	β [c]
2.2	0.044	3,900	130.7	29.8	1.008
3.0	0.305	4,554	853.3	5.34	0.833

[a] In units of h^{-1} Mpc
[b] $\alpha \equiv \frac{d_A(z)}{d_A\left(z_{[\mathrm{O\,II}]}\right)}$
[c] $\beta \equiv \frac{(1+z)H\left(z_{[\mathrm{O\,II}]}\right)}{\left(1+z_{[\mathrm{O\,II}]}\right)H(z)}$

Using Equation (A3) in Equation (A2) along with Equations (A4) and (A5), we find

$$P_{\mathrm{con}}\left(\boldsymbol{k}_\perp, k_\parallel\right) = \int \frac{d^2\boldsymbol{k}_\perp^{[\mathrm{O\,II}]}}{(2\pi)^2} \int d^2\boldsymbol{s}_\perp\, e^{i\left(\frac{\boldsymbol{k}_\perp^{[\mathrm{O\,II}]}}{\alpha} - \boldsymbol{k}_\perp\right)\boldsymbol{s}_\perp} \int \frac{dk_\parallel^{[\mathrm{O\,II}]}}{2\pi} \int ds_\parallel\, e^{i\left(\frac{k_\parallel^{[\mathrm{O\,II}]}}{\beta} - k_\parallel\right)s_\parallel} \times P_{[\mathrm{O\,II}]}\left(k^{[\mathrm{O\,II}]}\right)$$
$$= (\alpha^2\beta)\, P_{[\mathrm{O\,II}]}\left(\sqrt{\alpha^2 k_\perp^2 + \beta^2 k_\parallel^2}\right). \tag{A7}$$

This is the equation we use for computing the contamination of the LAE power spectrum. This result makes physical sense:

1. For a given set of values of $k_\perp$ and $k_\parallel$, we are actually observing the power spectrum of [O II] emitters at smaller scales, $k_\perp \to \alpha k_\perp$ and $k_\parallel \to \beta k_\parallel$. This contamination produces a horizontal shift of the [O II] power spectrum to smaller k values.

2. As the correlation function measures the dimensionless power spectrum, $k_\perp^2 k_\parallel P(k)$, the normalization of the power spectrum is also shifted by $\alpha^2\beta$, generating a vertical shift of the [O II] power spectrum.

At lower redshifts, α can be as large as 30 (see Table 5), which boosts the amplitude of the [O II] power spectrum by a factor of $\alpha^2 = 900$. Conversely, β is of order unity for the redshift range of interest.

Finally, the observed power spectrum is given by the weighted average of the LAE power spectrum, P_{LAE}, and the contamination power spectrum:

$$P_{\mathrm{obs}}\left(k_\perp, k_\parallel\right) = \left(1 - f_{[\mathrm{O\,II}]}\right)^2 P_{\mathrm{LAE}}\left(\sqrt{k_\perp^2 + k_\parallel^2}\right) + f_{[\mathrm{O\,II}]}^2 (\alpha^2\beta)\, P_{[\mathrm{O\,II}]}\left(\sqrt{\alpha^2 k_\perp^2 + \beta^2 k_\parallel^2}\right), \tag{A8}$$

where $f_{[\mathrm{O\,II}]}$ is the fraction of [O II] emitters in the total sample, i.e.,

$$f_{[\mathrm{O\,II}]} \equiv \frac{\text{number of contaminating [O II] emitters}}{\text{number of galaxies classified as LAEs}}. \tag{A9}$$

The contamination (the second term in Equation A8) makes the observed power spectrum *anisotropic*, even in the absence of redshift space distortions and the Alcock-Paczyński effect (Komatsu 2010).